Geophysical Research Letters

RESEARCH LETTER
10.1029/2023GL103695

Sea-Ice Impacts Inter-Annual Variability of Phytoplankton Bloom Characteristics and Carbon Export in the Weddell Sea

I. S. Giddy[1,2,3], S.-A. Nicholson[3], B. Y. Queste[2], S. Thomalla[1,3], and S. Swart[1,2]

[1]Department of Oceanography, University of Cape Town, Rondebosch, South Africa, [2]Department of Marine Sciences, University of Gothenburg, Gothenburg, Sweden, [3]Southern Ocean Carbon-Climate Observatory (SOCCO), CSIR, Cape Town, South Africa

Key Points:

- High-resolution in-situ observations are used to characterize multi-year phytoplankton bloom phenology and amplitude in the Antarctic Marginal Ice Zone
- Years with greater sea-ice volume drive deeper mixing that tend to support higher magnitude blooms in the northeast Weddell Sea
- Carbon export efficiency is affected by bloom magnitude, community composition and water column stratification

Supporting Information:

Supporting Information may be found in the online version of this article.

Correspondence to:

I. S. Giddy,
isabelle.giddy@gu.se

Citation:

Giddy, I. S., Nicholson, S.-A., Queste, B. Y., Thomalla, S., & Swart, S. (2023). Sea-ice impacts inter-annual variability of phytoplankton bloom characteristics and carbon export in the Weddell Sea. *Geophysical Research Letters*, *50*, e2023GL103695. https://doi.org/10.1029/2023GL103695

Received 15 MAR 2023
Accepted 22 MAY 2023

Abstract The Antarctic Marginal Ice Zone (MIZ) accounts for 15% of the Southern Ocean's primary production (PP), but limited data has hindered understanding of its variability and connection to carbon export. Using a combination of gliders, biogeochemical Argo floats and satellite observations in the northeast Weddell Sea, we show that years with more sea-ice formation over winter are followed by more intense phytoplankton blooms (~15% greater daily PP) and export to 100 m (~50% higher daily carbon export) the following summer. However, the carbon export beyond the deepest winter mixed layer did not vary in proportion to PP, suggesting different drivers of carbon export at depth compared to surface waters. Furthermore, across the entire MIZ, the response of blooms to sea-ice volume was spatially variable, indicating the need to consider spatial heterogeneity in the response of the biological carbon pump to future sea-ice changes.

Plain Language Summary Algae in the ocean surface take up carbon dioxide from the atmosphere through photosynthesis and transfer it to the deep ocean when they die and sink. This process is key to maintaining a habitable planet and is known as the biological carbon pump (BCP). The seasonally ice-covered ocean around Antarctica is one of the most active areas for algal growth, but also a region of rapid climate change. Because of the difficulty in taking measurements in this remote region, the physical and biological processes that control the growth and sinking of algae and its response to changing sea-ice remain uncertain. In this study, we use a combination of satellites and autonomous robots to elucidate the role of sea-ice variability on the BCP. We find that sea-ice impacts algal growth by its influence on both the light and nutrient conditions needed for photosynthesis. Predicting the amount of algae that subsequently sinks to depth as carbon flux, although influenced by sea-ice conditions, is more complex and linked to the greater marine ecosystem. Evidence suggests that the species of algae, zooplankton grazing, and the rate at which dead algae breaks down and sinks are important and should be a focus point for further research.

1. Introduction

The Antarctic Marginal Ice Zone (MIZ) undergoes the surface ocean's largest transformation by the annual growth and retreat of sea-ice (Parkinson, 2019). One of the most productive oceanic regions (Ardyna et al., 2017; Arrigo et al., 2008), the MIZ accounts for ~15% of Southern Ocean (SO) primary production (PP) (Taylor et al., 2013), that supports a diverse food-web dominated by krill, marine birds, seals and whales (Massom & Stammerjohn, 2010), and drives the biological carbon pump (BCP) by mediating the downward transport of particulate organic carbon (POC) from the surface ocean to the interior.

The phenology of phytoplankton blooms in the Antarctic MIZ has been relatively well-observed since the satellite era and the introduction of under ice biogeochemical Argo (BGC-Argo) floats (Ardyna et al., 2017; Arteaga et al., 2020; Thomalla et al., 2011; Uchida, Balwada, Abernathey, Prend, et al., 2019; von Berg et al., 2020). In the Antarctic MIZ, the seasonal range of PP (difference between mean winter and summer chl-*a* concentrations) is 2–3 times greater than in other SO regions in response to the high seasonality of solar irradiance and sea-ice (Ardyna et al., 2017). Although blooms initiate while still under light-limiting conditions (<1 Ein m^{-2} day^{-1}) (Arteaga et al., 2020; Hague & Vichi, 2021), sea-ice melt enhances the rate of PP by generating a shallow freshwater lens and retaining phytoplankton in a higher average light environment (Lester et al., 2021; Smith & Comiso, 2008; Smith & Nelson, 1985; Thomalla et al., 2011). Ice melt also deposits iron (Arrigo et al., 2008; Lannuzel et al., 2016), which can temporarily enhance PP. However, in the SO, the major supply of iron is from depth, when winter mixing deepens the mixed layer beyond the ferricline and entrains a large reservoir of iron

to support seasonal growth (Ardyna et al., 2017; Llort et al., 2015; Nicholson et al., 2016, 2019; Tagliabue et al., 2014).

PP is connected to the export of POC into the ocean interior through biological and physical processes, with only a small fraction of the organic carbon fixed by PP in the surface ultimately reaching the ocean interior (Giering et al., 2014; Henson et al., 2019; Martin et al., 1987). The BCP describes a suite of pathways through which organic particles are exported from the surface layer to depth (Boyd et al., 2019). These include sinking via the gravitational pump or direct transport through the physical injection pump (Omand et al., 2015) as well as via feeding by vertically migrating organisms (Stukel et al., 2023). While all pathways are likely to contribute to export in the MIZ, the depth of the mixed layer during summer is stable as a result of strong stratification by sea-ice melt, suppressing vertical transport along isopycnals by submesoscale flows (Giddy et al., 2021) and thus hindering the role of the physical injection pump. The gravitational pump is therefore thought to be more important in driving carbon export in this region, with most export occurring toward the end of the bloom season (Moreau et al., 2020). The export efficiency of the gravitational pump is regulated by particle formation and rates of sinking (aggregation, fragmentation, ballasting) and remineralization (microbial activity, chemical dissolution), senescence, grazing and viral lysis, themselves all factors that largely depend on rates of PP and community composition (Bach et al., 2019; Henson et al., 2019).

Globally, the upper ocean is predicted to continue to stratify into the 21st century (Kwiatkowski et al., 2020; Sallée et al., 2021). In the Antarctic MIZ, the resultant reduction in vertical nutrient fluxes may decrease PP (Arteaga et al., 2020), but conversely, decreased sea-ice cover may lengthen the bloom season and increase net PP (Henson et al., 2021). Sinking organic carbon that is remineralized within the Circumpolar Deep Water layer accounts for about half of the carbon sink in the Weddell Sea (MacGilchrist et al., 2019; Naveira Garabato et al., 2017), suggesting that changes in the BCP here can have a disproportionate impact on the global carbon cycle. However, how changes in PP translate to POC export from subseasonal to interannual timescales in the Antarctic remains unclear and an area of active research (e.g., Arteaga et al., 2020; Belcher et al., 2019; Henson et al., 2023; Moreau et al., 2020).

This study aims to examine the link between PP and carbon export in the SO MIZ. We focus on a region in the North Eastern Weddell Sea (Figures 1a and 1b) that is covered by sea-ice in the winter and has a strong seasonal bloom in summer. First, we harness two decades of satellite observations and two profiling SOCCOM BGC-Argo floats to contextualize two years of phytoplankton blooms observed between 2018 and 2020, at sub-daily resolution using gliders (referred to as SG2018 and SG2019 respectively; Figures 1c and 1d). We highlight interannual variability in bloom phenology and amplitude and propose a likely physical control mechanism. Second, we use the glider data to link the biological and physical processes that control the export of POC to the underlying Upper Circumpolar Deep Water (UCDW), from where dissolved organic carbon has the potential to be sequestered into the ocean's abyss (Hoppema, 2004; MacGilchrist et al., 2019).

2. Methods

All data used and their processing is described in Texts S1 and S2 in Supporting Information S1.

2.1. Phenology Metrics

We describe phytoplankton blooms by duration (days) and magnitude in the northeast Weddell Sea using 23 years of satellite observations together with two SOCCOM floats (WMO ID:5904397 and 5904467) that were profiling near to the glider deployment location between 2015 and 2020.

The presence of sea-ice limits the ability to detect bloom initiation using only satellite observations of chl-*a*. Therefore, we do not attempt to detect true bloom initiation, but rather the point at which the bloom starts to rapidly accumulate toward its seasonal maximum. To do this, we first assess the bloom peak (maximum magnitude) as the annual chl-*a* maximum, wherein an annual cycle is defined from July to the following June. We then identify the seasonal ramp as the point at which the bloom reaches 50% of its maximum. Bloom termination is defined using a chl-*a* threshold, following Hopkins et al. (2015), where bloom termination is the postpeak minimum concentration plus 5% of the range between the peak and postpeak minimum concentration. An adjusted bloom duration is determined as the number of days between the seasonal ramp and termination. Since integrated

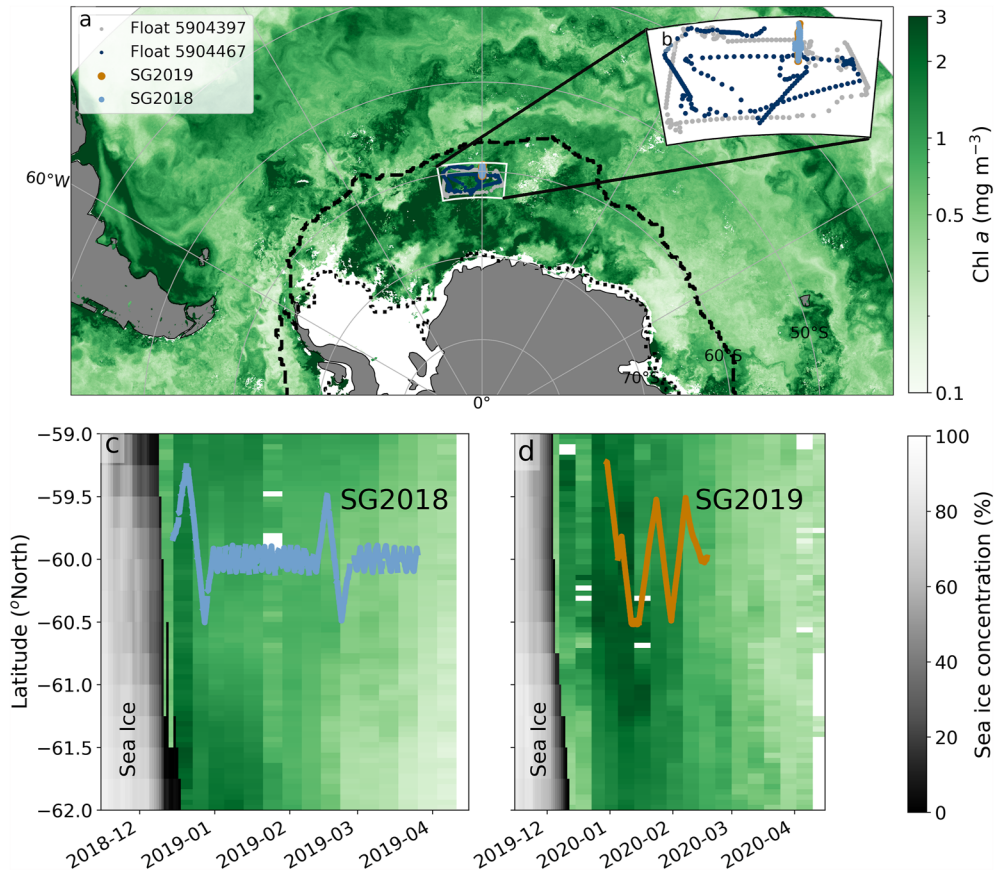

Figure 1. (a) Average satellite chlorophyll-*a* concentration (Ocean Color-Climate Change Initiative) during austral summer (December 2019–Feburary 2020) in the Atlantic sector of the Southern Ocean. The maximum and minimum sea-ice extents (National Snow and Ice Data Center) are shown in the dashed and dotted black lines, respectively. The study region is demarcated by the inlaid white box (b), which shows the sampling trajectories of the two SOCCOM floats WMO ID:5904397 (during 2015–2020, dark blue) and WMO ID:5904467 (during 2014–2019, gray), and the two Seagliders (SG2018, during December 2018–March 2019, light blue) and SG2019 (December 2019–Feburary 2020, orange). (c) Hovmöller plot for the latitudinal extent (averaged across longitude) of the study region of sea-ice concentration (Sea-ice Concentration Climate Data Record, OSI 430b) and satellite chlorophyll-*a* during the (c) 2018–2019 summer season for the SG2018 deployment (latitudinal trajectory shown in blue), and (d) for the 2019–2020 summer for the SG2019 deployment (orange).

chl-*a* over the bloom duration was linearly correlated with bloom magnitude, (Figure S1 in Supporting Information S1; $r^2 = 0.7$; $p < 0.001$), we use only bloom magnitude and duration as the key metrics characterizing interannual bloom variability.

2.2. Seasonal Physical Environmental Conditions

Here we define key metrics used to characterize physical environmental conditions of the study region. The onset of sea-ice melt is defined as the date when sea-ice concentration first decreased and remained below 85% of the annual maximum. As a proxy for sea-ice growth, mean annual sea-ice volume is computed as ice area (from sea-ice concentration) multiplied by the ice thickness, and averaged in time. While this metric carries uncertainty, both in the satellite products (ice thickness is limited to 50 cm and therefore likely to underestimate true ice thickness), and in the assumed linear relationship between ice growth and ice volume, in lieu of other observations we take this as a reasonable first approximation. A threshold for seasonal wind increase is defined as the first day in which wind stress reached 10% greater than the median wind stress after the annual minimum wind stress (using the same definition for an annual cycle as in Section 2.1). The day when net heat flux (Q_{net}) rises above (drops below) +10 W m^{-2} (positive into the ocean/negative out of the ocean) is also compared to bloom initiation and termination. Photosynthetically Active Radiation (PAR) is correlated with net heat flux ($r^2 = 0.86$; Figure S2

in Supporting Information S1) so is not assessed separately. For the analysis of bloom phenology, sea-ice and atmospheric variables are averaged to the same temporal resolution as the satellite chl-*a* observations (8-day) and all satellite products are averaged within the bounding box indicated in Figure 1b (−10 to 5°E and −62 to −59°S). For the extended analysis of the drivers of bloom magnitude, we use a snapshot of all SOCCOM floats that profiled in the MIZ between 2012 and 2022 (Johnson et al., 2022). Data are averaged into 5° × 2° longitudinal and latitudinal bins. For comparison with the floats, sea-ice and ocean color observations are similarly binned. When comparing only sea-ice and satellite chl-*a* observations we use 1° × 1° bins.

The mixed layer depth (MLD) is defined as the depth at which the density changes by 0.03 kg m^{-3} compared to a reference density within the mixed layer, at 10 m (de Boyer Montégut, 2004). MLD_{max} is the annual winter mixed layer maximum derived from the SOCCOM floats.

2.3. Primary Production

PP is estimated using the spectrally resolved Carbon-based Productivity model (CbPM; Westberry et al., 2008; Arteaga et al., 2022) applied to the glider profiles (see Figure S3 in Supporting Information S1 for full sections of chl-*a* and phytoplankton carbon, C_{phyto} and Figure S8 in Supporting Information S1 for PP model comparisons). The CbPM estimates PP as a function of carbon biomass and phytoplankton growth rate. Carbon is estimated from optical backscatter using empirical relationships previously measured in the SO: $C_{phyto} = 0.19 \times POC + 8.7$ (Graff et al., 2015) and $POC = 9.776 \times 10^4 \times bbp_{700}^{1.166}$ (Johnson et al., 2017), where bbp_{700} is the optical backscattering at 700 nm (see Text S1 in Supporting Information S1). Growth rate is estimated from the chl-*a*:C_{phyto} ratio and surface PAR. However, glider PAR was only available during the 2018 deployment (SG2018). To extend the PP analysis to the 2019 glider deployment (SG2019), Moderate Resolution Imaging Spectrometer/Aqua (MODIS) satellite PAR was co-located with both gliders. Glider PAR was comparable with satellite PAR ($r^2 = 0.44$, gain = 0.9; Figure S4 in Supporting Information S1) giving us confidence to use satellite PAR during SG2019 when no in situ PAR was available.

2.4. Aggregate Particulate Organic Carbon Export

We use high resolution optical backscatter measurements from the gliders to estimate POC export. Glider backscatter profiles are separated into a "small" particle baseline signal (7-point running minimum followed by a running maximum) and a "large" particle "spike" signal (all residuals above the baseline), following Briggs et al. (2011). After bin-averaging profiles of backscatter in the vertical to 10 m with a 50 m rolling mean, and binning profiles to 2-day with a 2-day running mean in time, carbon flux events are identified as follows. First, using a 10-day moving window over each glider data set, the time of maximum spike for each depth level is identified. Linear regressions are then fitted between the depth of each maximum spike and time. Only regressions with $r^2 > 0.4$ are identified as flux events. Application of a rolling window together with the r^2 threshold reduces the chances of false identification of advection events as flux events. Finally, the linear regression fits are used to estimate the sinking speed of large particles (Δdepth/Δtime) (Figure S5 in Supporting Information S1). Large particle backscatter is converted to POC, and multiplied by the derived bulk sinking speeds (with individual export events ranging between 48 and 88 m day^{-1} and an average sinking rate of 65 m day^{-1}) to estimate aggregate POC flux (Equation 4, Briggs et al., 2011). Export is estimated at 100 m, as the depth horizon most commonly used to estimate export in models (Buesseler & Boyd, 2009) and at E_z, defined as the depth where chl-*a* drops to 10% of its maximum (for further discussion see Buesseler et al., 2020). Export efficiency (E_{eff}) is defined as the ratio of export at 100 m to PP, using PP values from 2 days earlier. The 100 m depth horizon is chosen to estimate export efficiency for comparison to previous studies. A lag of 2 days was chosen based on the average sinking rates of aggregates. Similarly, transfer efficiency (T_{eff}) is defined as the ratio of export at 170 m (the average deepest winter mixed layer, Moreau et al., 2020) to export at 100 m from 2 days earlier. We also estimate T_{eff} from the rate of flux attenuation by fitting the aggregate POC profiles identified as export events to Martins Curve (Martin et al., 1987):

$$F_z = f_{z_0} \times (z/z_0)^{-b}, \quad (1)$$

where F_z is the carbon flux with depth, f_{z_0} is the flux at a reference depth z_0, z is depth, and b is the attenuation coefficient, with smaller $-b$ representing faster attenuation rates and a lower T_{eff}. We use a variable reference depth determined by the depth of E_z.

3. Results and Discussion

3.1. Characteristics and Drivers of Variability of the Seasonal Bloom in the Weddell Sea

The efficiency of the BCP is associated with the characteristics of the seasonal bloom, that are mediated by nutrient availability, light and mortality (Arteaga et al., 2018; Behrenfeld & Boss, 2014). We assess the drivers of bloom phenology and amplitude in the northeastern Weddell Sea to determine what sets the upper limits of PP in this region. Ocean color, float and glider observations of chl-*a* describe the MIZ summer bloom (Figure 2a), with the average bloom ramp occurring in mid-December, and termination in mid-March. Although the mean phenology of all three products is in agreement, we note the offset in chl-*a* magnitude between ocean color derived chl-*a* and chl-*a* derived from the WET Labs ECO series fluorometers on floats and gliders (Roesler et al., 2017). Results show a close correspondence in the timing of sea-ice melt and the bloom ramp, with 50% of the seasonal bloom ramp attributed to the onset of ice melt (i.e., when some ice melt has occurred, Figures 2a and 2b; Figure S6a and S6b in Supporting Information S1), similarly noted by von Berg et al. (2020). This highlights the important role of stratification (by the melt of sea-ice) in driving a high light environment for sustained net growth needed to accumulate biomass. The timing of bloom termination was more variable and less predictable. We assessed the seasonally variable physical parameters of wind stress, PAR, heat flux, and autumn ice formation as potential drivers, but found no significant correlations with the timing of bloom termination (Figure 2b, Figures S6c and S6d in Supporting Information S1). As such, we conclude that bloom termination is most likely driven by the depletion of nutrients and trace metals (Boyd et al., 2005; Krause et al., 2019), grazing (Kauko et al., 2021; Moreau et al., 2020), bacteria, and viruses (Biggs et al., 2021), which were not measured as part of this study.

By far the most prominent characteristic of interannual variability in the seasonal cycle is that of bloom magnitude, which ranged from a very meager seasonal maximum of 0.4 mg m^{-3} (2010) to a seasonal maximum of 2.8 mg m^{-3} (2005), when observed across a 23 years satellite record from 1997 to 2020 (Figure 2a, dark green line). We hypothesize that years with a higher sea-ice concentration and volume will drive higher magnitude blooms as previously suggested by Ardyna et al. (2017) by enhancing iron supply either from ice melt (Arrigo et al., 2008; Lannuzel et al., 2016) or winter mixing, driven by brine rejection during sea-ice growth (McPhee & Morison, 2001; Wilson et al., 2019). To test this hypothesis in our region of interest (northeast Weddell Sea), we compute the correlations between ice volume, the deepest winter mixed layer depth (MLD_{max}) and bloom magnitude (Chl_{max}). Although a robust statistical analysis is limited by the small sample size ($n = 5$ years), we find strong positive correlations between MLD_{max} and Chl_{max} ($r^2 = 0.9$; $p < 0.1$, Figure 2c) and MLD_{max} and ice volume ($r^2 = 0.69$; $p < 0.1$; Figure 2d), which suggests that the degree of deep winter mixing, itself influenced by sea-ice growth, drives interannual variability in Chl_{max}. This relationship is plausible given the shallow reservoir of dissolved iron as UCDW upwells (located between 100 and 200 m in the winter) in the northern edge of the Weddell Sea (Klunder et al., 2011). The weaker positive correlation between ice volume and Chl_{max} ($r^2 = 0.36$; $p = 0.2$, Figure 2e) suggests that direct supply of iron and/or enhanced light supply from ice melt is less likely to play a prominent role in driving bloom amplitude in this region.

Expanding this analysis to the entire ice covered SO using the full ocean color satellite record of sea-ice concentration and chl-*a* (1997–2022), we find that years with higher sea-ice concentration elicit both weak positive (28%; $p < 0.1$) and negative (23%; $p < 0.1$) response in Chl_{max} that varies regionally (Figure 2i). Similar regional variability is observed in the response of chl-*a* to mean annual ice volume (used as a proxy for ice growth) from SOCCOM floats (Figure 2h). Notably, regions with a negative correlation between sea-ice concentration and Chl_{max} tend to be constrained to shallow bathymetric features, for example, Maud Rise (65°S, 3°E), which are typically less iron-limited than deep open-ocean regions.

In contrast to Li et al. (2021), we find evidence of a mechanistic link between winter mixing and Chl_{max} (Figures 2c and 2f), albeit inconsistent across all regions characterized by a positive bloom response to sea-ice volume (Figure 2h). The spatial heterogeneity in these relationships is nonetheless expected inlight of recognised regional variability in the dominant drivers of seasonal iron and/or light limitation. In cases where a negative response is observed in Chl_{max} to winter MLD_{max}, light may instead be limiting (Ardyna et al., 2017), or the ferricline deeper than the depth of winter mixing (Carranza & Gille, 2015; Fauchereau et al., 2011). Similarly, in those instances where enhanced ice volume does not result in deeper winter mixing (Figure 2g), it is possible that sea-ice was advected and not formed locally. In addition, depending on the ambient stratification, winter mixing will have varying levels of sensitivity to ice growth (Wilson et al., 2019). Alternative mechanisms of iron supply may also confound the relationships observed between ice volume—winter mixing (Tagliabue et al., 2014) and

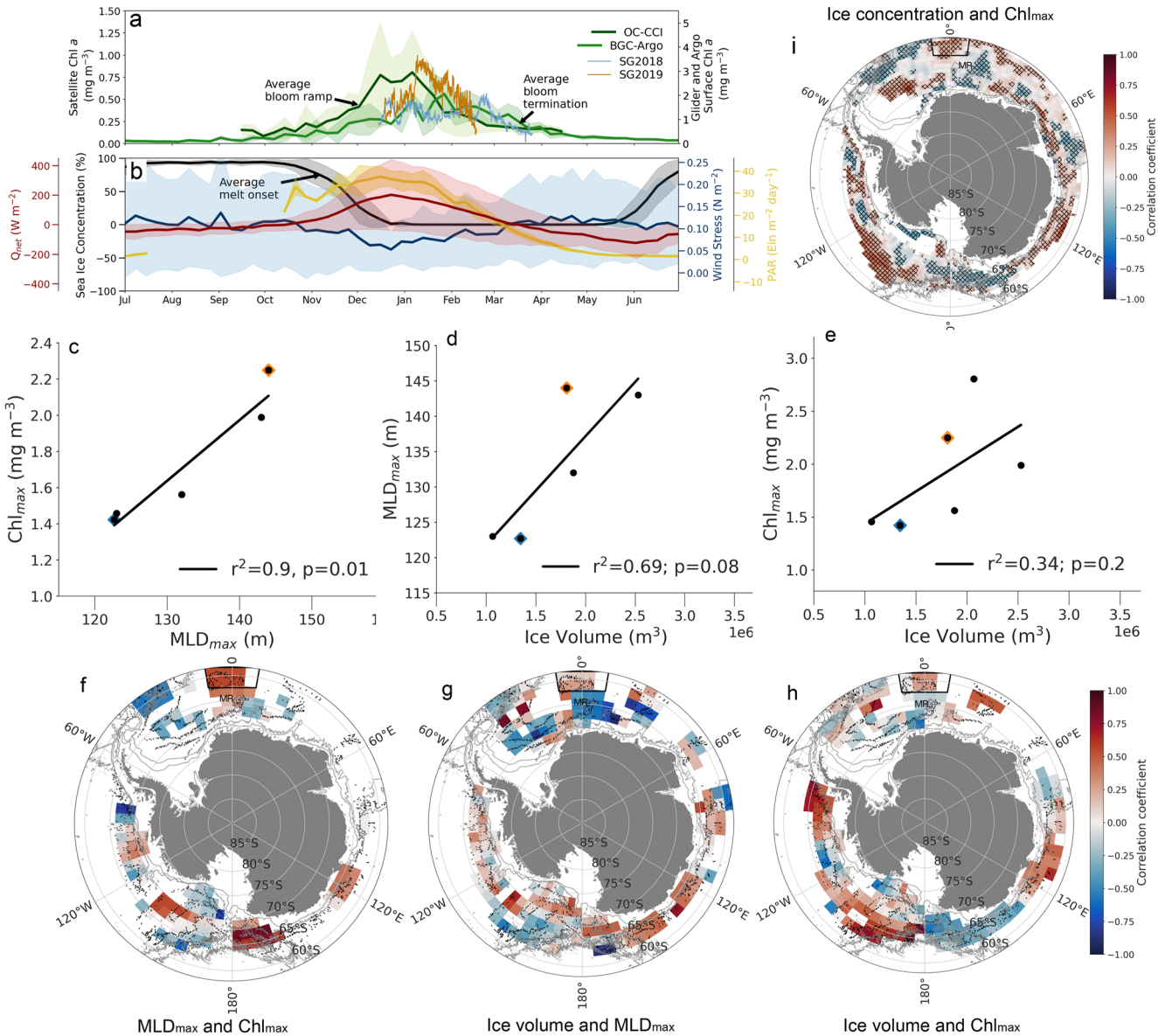

Figure 2. (a) Climatologies of satellite-observed surface chl-*a* (OC-CCI; 1997–2020, dark green) and mean of two SOCCOM floats during overlapping years (2015–2019; WMO IDs: 5904467 and 5904397; light green). Glider observations of surface chl-*a* during the 2018-2019 summer season (light blue, SG2018) and the 2019-2020 summer season (orange, SG2019). Float and glider chl-*a* are averages over the upper 40 m. Note the different *y*-axis scales for satellite observations compared with glider/float observations. The climatological bloom ramp and termination dates are indicated (based on OC-CCI data). (b) Climatologies over the same time period of sea-ice concentration (black), Qnet (red), wind stress (blue) and Photosynthetically Active Radiation (yellow). The sea-ice melt onset is indicated. Shading in panels (a and b) represent one standard deviation. Linear regressions of (c) yearly averages of the deepest winter mixed layer with the following summers' maximum chl-*a* (Chl_{max}) as observed by the SOCCOM floats (2015–2019); (d) the total annual ice volume with the deepest winter mixed layer (2015–2019) and (e) the annual ice volume with Chl_{max} as observed by the SOCCOM floats (2015–2019). Yearly averages of the two SOCCOM floats that were within the study region are shown. The years that coincide with the glider deployments are depicted in light blue (2018) and orange (2019). (f, g, h) The same as (c, d, e) but presented as a map of all available SOCCOM floats (2012–2022). The locations of SOCCOM floats appear as black dots. Colormaps show the Pearson's *r* correlation coefficient. (i) Map of the correlation between sea-ice concentration and Chl_{max} from 1997 to 2022. Pixels where $p < 0.1$ are hashed in (i). ETOPO Global Relief Model bathymetry is contoured (1,000, 2,000, 3,000 m) in gray. The study region is outlined with a black box, and Maud Rise (65°S, 3°E) is labeled MR.

the extent of seasonal blooms. For example, iron supplied by hydrothermal vents can drive anomalously large blooms (Ardyna et al., 2019). The characteristics of summer storms can have both a positive impact on Chl_{max} by intermittently supplying iron (Moreau et al., 2023; Nicholson et al., 2019) or a negative impact by reducing available light (Fitch & Moore, 2007). Although the potential for vertical supply of iron by submesoscale flows (Uchida, Balwada, Abernathey, McKinley, et al., 2019) was found to be weak in our specific region of interest

(due to the strongly stratified ocean following ice melt, Giddy et al., 2021), this may not be the case for all of the ice impacted SO, in particular those regions characterized by weaker stratification and deeper mixed layers (Biddle & Swart, 2020; Timmermans et al., 2012). Indeed, while the sea-ice zone was not included in their analysis, Prend et al. (2022) found that intraseasonal (submesoscale) variability in SO chl-*a* was the primary determinant of inter-annual variability in mean chl-a. In years and regions where the above discussed mechanisms are active or dominant, a decoupling of Chl_{max} from MLD_{max} and ice volume would be expected.

3.2. The Fate of Particulate Organic Carbon

We link surface processes to the fate of sinking organic carbon by coupling the analysis of phytoplankton phenology and amplitude in Section 3.1 to two distinct years of seasonal blooms (Figure 2a) that were observed by gliders (Figure 1, SG2018 and SG2019). For this analysis, we treat the gliders as Lagrangian, assuming that the advective term is small. The bloom captured by SG2018 was longer and of a lower magnitude (Chl_{max} = 2.0 mg m^{-3}, 101 days), while in contrast, the bloom captured by SG2019 was shorter and of higher magnitude (Chl_{max} = 3.7 mg m^{-3}, 85 days of which the glider sampled 51 days, Figures 1c and 1d, 2a; Figure S3 in Supporting Information S1). Correspondingly, MLD_{max} was 20 m deeper preceding the higher magnitude bloom in 2019 compared with 2018 (Figure 2c).

Modeled rates of PP reflect the characteristics of surface chl-*a* (Figure 1a), and were ∼15% lower during 2018–2019 (1488 ± 438 mg C m^{-2} day^{-1}, Figure 3a) compared to 2019–2020 (1731 ± 403 mg C m^{-2} day^{-1}; Figure 3b). Differences in PP between the two years translated into even bigger differences (∼50%) in daily export rates at 100 m (86 ± 40 mg C m^{-2} day^{-1}, E_{eff} = 0.07 ± 0.0 and 195 ± 70 mg C m^{-2} day^{-1}, E_{eff} = 0.11 ± 0.03 respectively, Figures 3a and 3b; Figure S7b in Supporting Information S1). When we extended this analysis to T_{eff} ($export_{170m}$:$export_{100m}$), we found that T_{eff} was inverted, with a higher T_{eff} in 2018–2019 (0.46 ± 0.11) than in 2019–2020 (0.26 ± 0.09; Figure S7c in Supporting Information S1); a result also reflected in the flux attenuation rate, which was smaller in 2018–2019 (−1.4 ± 0.4) than in 2019–2020 (−2.2 ± 0.1, Figure 3g). This translates to similar daily export rates to 170 m between the two years despite substantial differences in PP and export at 100 m (2018–2019: 38 ± 20 mg C m^{-2} day^{-1} and 2019–2020: 48 ± 16 mg C m^{-2} day^{-1}; Figures 3a and 3b). Replacing E_{100m} with E_z changes the quantitative estimates of E_{eff} and T_{eff} but the relative patterns of difference between the two years of interest remain the same. To summarize, the bloom observed in 2018–2019 was characterized by lower PP and lower E_{eff} while the bloom observed in 2019–2020 was characterized by higher PP and higher E_{eff}. However, both blooms had similar T_{eff}.

Substantial interannual variability observed in flux attenuation rates (Figure 3g) suggest that remineralization rates, which are known to account for a large proportion of variability in T_{eff} (Bach et al., 2019; Belcher et al., 2016), contrasted across the 2 years (regardless of choice of export depth horizon as 100 m or E_z) and may explain the similarity in export at 170 m, despite differences in PP. The rate of remineralization is primarily controlled by (a) temperature (Marsay et al., 2015), (b) variation in sinking rates associated with size and porosity of aggregates (Bach et al., 2019) and the ratio between particle and water density (Condie, 1999), and (c) microbial degradation influenced by functional activity and community structure, as well as POC composition (labile, semi-labile, recalcitrant) (Cavan et al., 2018) and (d) grazing load (Cavan et al., 2015; Henson et al., 2019). Although at a global scale variations in temperature are known to be a key driver of regional differences in attenuation (Marsay et al., 2015), we assume the effect of temperature is negligible as interannual variability is small compared to latitudinal variability (Figures 3c and 3d).

As expected, a deeper winter MLD prior to the summer bloom would likely result in an increase in iron supply, thereby supporting a higher magnitude bloom as seen in 2019–2020 (Figures 2c and 2d). A typical community composition response to high iron and light availability would be a dominance of diatoms (Smetacek et al., 2012; Tréguer et al., 2018), that would be expected to sink faster with their additional ballast, escaping microbial degradation and hence drive a higher T_{eff} and lower attenuation rate. Although we did not directly measure community composition, chl-*a*:C_{phyto} ratios have been used to infer changes in community composition (Cetinić et al., 2015). A lower chl-*a*:C_{phyto} ratio in 2018–2019 suggests iron limiting conditions. As such, there were likely more diatoms (that have higher iron requirements) in the community during 2019–2020 than during 2018–2019. However, the sinking rates were not significantly different between the two years (65 m day^{-1}; Figure S5 in Supporting Information S1), and the presumptive diatom-dominated bloom was counter-intuitively characterized by a faster attenuation rate (Figure 3g).

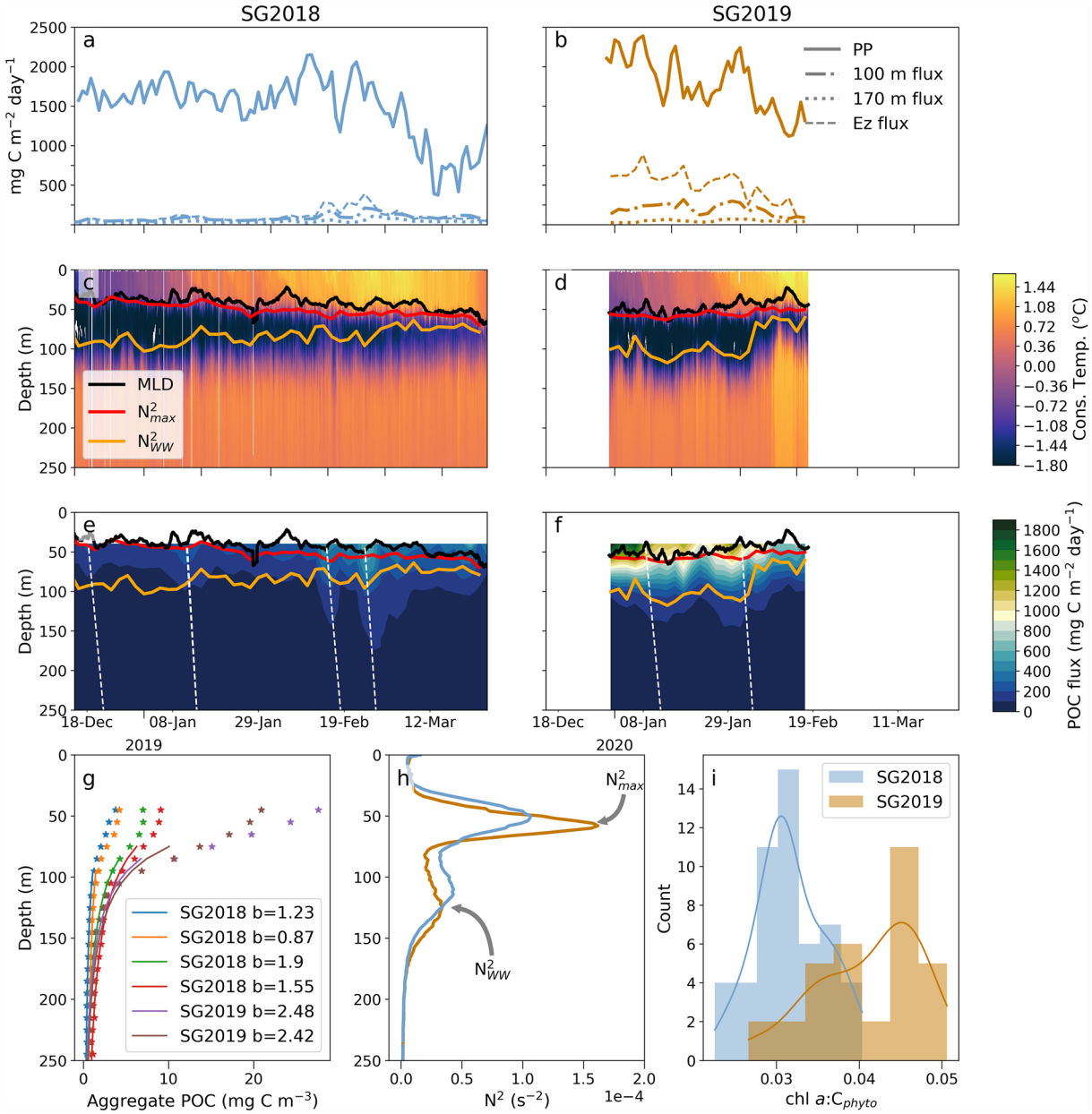

Figure 3. (a) Integrated primary production in the upper 200 m smoothed by 4 days (solid line), export at Ez, the base of the euphotic zone (dashed line), export at 100 m (dash-dot line) and export at 170 m (dotted line) from glider deployments in (a) the 2018–2019 and (b) the 2019–2020 productive seasons. Vertical sections of conservative temperature in (c) 2018–2019 and (d) 2019–2020. Marked on (c, d, e, f) are the mixed layer depth (black line), the depth of maximum stratification (N^2_{max}) (red line), and the depth of the Winter Water N^2_{max} (orange line). Vertical sections of large particle Particulate Organic Carbon flux during (e) 2018–2019 and (f) 2019–2020. Values above 40 m are missing as a result of the 50 m rolling mean applied to the data set (see Section 2.4). Flux events are identified with the white dashed lines. (g) Martin Curve fits during flux events. (h) Mean vertical stratification profiles corresponding to SG2018 (blue) and SG2019 (orange). (i) Histograms of average mixed layer chl-*a*:C_{phyto} ratio in SG2018 and SG2019.

Changes in density with depth can also influence the sinking rate of particles through two mechanisms. Firstly, when a sinking particle encounters denser water, the relative density between water and particle is reduced and the buoyancy force on the particle increases, decreasing its sinking velocity (Condie, 1999). Secondly, under conditions where the thermocline deepens at a rate faster than the sinking speed of the particles, particles may be re-entrained into the mixed layer (Lacour et al., 2019; D'Asaro, 2008; Noh & Nakada, 2010). If, through these mechanisms, particles are retained within the thermocline, they would be exposed to a longer period of remineralization in the upper ocean, thus reducing export to depth. Indeed, the accumulation of particles within the

thermocline is a strong feature of the bloom in 2019–2020 (Figure 3f), and particles appear to follow isopycnals, while those in 2018–2019 do not (Figure 3e). Additionally, the level of stratification in 2019–2020 is greater than in 2018–2019 (N^2_{max} = 1.6 × 10^{-3} s^{-1} and 1.0 × 10^{-3} s^{-1}, respectively; Figure 3h). While a diatom-dominated community might be expected to sink faster, the larger density change with depth observed in 2019–2020 may slow particle sinking rates, resulting in the relatively similar sinking rates observed across the two years and the reduced T_{eff} for 2019–2020.

Finally, remineralization rates and flux attenuation may be influenced by grazing (e.g., Cavan et al., 2015). Thus, the faster remineralization rates observed in 2019–2020 could be a result of higher grazing pressure within the upper 200 m. This is feasible as grazing by zooplankton has been demonstrated to account for ∼90% of the fate of phytoplankton in this region (Moreau et al., 2020), although grazing is not constrained in this study.

The above discussion demonstrates the additional need for biological observations from for example, imaging systems, sediment traps or remote access samplers allowing optical or traditional microscope and genetic methods to distinguish the community and better attribute drivers of the observed variability in export.

4. Conclusions

Glider measurements of both physical (temperature and salinity) and biological (chl-*a* and carbon) variables enable the simultaneous quantification of PP, export, and water column stratification at scales of hours to days. These results, complemented by float and satellite observations, reveal the complexity of interactions influenced by the sea-ice characteristics (formation, duration, melt) that currently govern PP and carbon export in the SO MIZ. Taking a case study approach, we first find empirical evidence in the northeast Weddell Sea that increased winter sea-ice formation drives deeper winter mixing, which in turn leads to more intense phytoplankton blooms in the following season, likely due to iron entrainment. Expanding this analysis to all available float data in the MIZ reveals spatially variable responses of blooms to both sea-ice formation and winter mixing, highlighting the complexity of bloom response to multiple top-down and bottom-up drivers. Despite the spatial heterogeneity, we observe coherent regions in parts of the Ross Sea and East Antarctic sector (Figure 2i) whose bloom characteristics are susceptible to changes in sea-ice conditions. The highly variable response of phytoplankton to physical drivers in the dynamic sea-ice zone of the SO calls for targeted multi-season process studies that focus on the different regimes that were evident in this study (e.g., open ocean, shallow bathymetry, strongly stratified vs. weakly stratified). The integration of shear probes on profiling floats under sea-ice would constrain uncertainties related to the turbulent flux of PP limiting nutrients (e.g., Schulz et al., 2022). Furthermore, sensitivity tests with a coupled biogeochemical model are needed to better quantify the mechanistic link between sea ice growth, winter mixing and phytoplankton growth as well as develop an understanding of the role of advective terms (both of sea ice and subsurface).

Secondly, our two seasons of glider observations provide preliminary evidence of higher carbon export at 100 m (higher E_{eff}) associated with more intense blooms related to enhanced ice growth in the winter and its subsequent melt in summer. The implication is that with increased variability and the predicted reduction in sea-ice growth that results from a warming climate, carbon export to depth may decrease on seasonal timescales, affecting the mesopelagic and the BCP. However, variability in attenuation rates and T_{eff} meant that higher export at 100 m did not necessarily translate into substantially higher export past 170 m, the depth of deepest winter mixing. We attribute the decoupling between E_{eff} and T_{eff} to both physiological differences associated with differing phytoplankton community compositions in response to differences in iron availability and to changes in stratification associated with ice melt. These findings suggest asynchronous inter-annual variability in the drivers of carbon export compared to PP.

Data Availability Statement

All data used in this study is freely available online. Biogeochemical Argo data were collected and made freely available by the Southern Ocean Carbon and Climate Observations and Modeling (SOCCOM) Project funded by the National Science Foundation, Division of Polar Programs (NSF PLR -1425989 and OPP-1936222), supplemented by NASA, and by the International Argo Program and the NOAA programs that contribute to it. The Argo Program is part of the Global Ocean Observing System. The snapshot used was taken on 2022-05-19 (Johnson et al., 2022) and is available at the following DOI:https://doi.org/10.6075/J0MC905G. The results in this paper

contain modified Copernicus Climate Change Service information 2021. Neither the European Commission nor ECMWF is responsible for any use that may be made of the Copernicus information or data it contains. The glider data is archived with the National Center for Environmental Information and is available at the following url https://www.ncei.noaa.gov/access/metadata/landing-page/bin/iso?id=gov.noaa.nodc:0244004. The code that was used in the analysis of this paper is accessible via Zenodo: https://doi.org/10.5281/zenodo.5655923. The code used to compute the glider-CbPM was adapted from L. Arteaga's script available on Github: https://zenodo.org/badge/latestdoi/368542675.

Acknowledgments

This work was supported by the following grants of S. Swart: Wallenberg Academy Fellowship (WAF 2015.0186), Swedish Research Council (VR 2019–04400); S.Swart and S. Thomalla: STINT-NRF Mobility Grant (STNT180910357293); S.-A. Nicholson and S. Swart are supported by the European Unions Horizon 2020 research and innovation programme under Grant 821001 (SO-CHIC) and the NRF-SANAP (SNA170522231782, SANAP200324510487); S.Thomalla: CSIR Parliamentary Grant. B. Queste was supported by NSFGEO-NERC: Collaborative Research: Accelerating Thwaites Ecosystem Impacts for the Southern Ocean (ARTEMIS, Grant 1941483). I.S Giddy acknowledges the support of the NRF-SANAP (SNA170506229906) and iAtlantic Horizon 2020 Grant (818123). This work would not have been possible without the valuable fieldwork aboard the RV SA Agulhas II, her captain and crew for deployment of gliders; Andy Thompson and the glider piloting team at Caltech for their contributions to the ROAM-MIZ project, including glider SG643 and its associated data. The authors would like to thank Nathan Briggs for advice regarding the calculation of particulate organic carbon export, Hannah Joy-Warren for feedback at the final stages of the manuscript and the three anonymous reviewers whose constructive comments contributed to the improvement of this manuscript.

References

Ardyna, M., Claustre, H., Sallée, J.-B., D'Ovidio, F., Gentili, B., van Dijken, G., et al. (2017). Delineating environmental control of phytoplankton biomass and phenology in the Southern Ocean: Phytoplankton Dynamics in the SO. *Geophysical Research Letters*, *44*(10), 5016–5024. https://doi.org/10.1002/2016GL072428

Ardyna, M., Lacour, L., Sergi, S., d'Ovidio, F., Sallée, J.-B., Rembauville, M., et al. (2019). Hydrothermal vents trigger massive phytoplankton blooms in the Southern Ocean. *Nature Communications*, *10*(1), 2451. https://doi.org/10.1038/s41467-019-09973-6

Arrigo, K. R., van Dijken, G. L., & Bushinsky, S. (2008). Primary production in the Southern Ocean, 1997–2006. *Journal of Geophysical Research*, *113*(C8), C08004. https://doi.org/10.1029/2007JC004551

Arteaga, L., Behrenfeld, M. J., Boss, E., & Westberry, T. K. (2022). Vertical structure in phytoplankton growth and productivity inferred from biogeochemical-argo floats and the carbon-based productivity model. *Global Biogeochemical Cycles*, *36*(8). https://doi.org/10.1029/2022GB007389

Arteaga, L., Boss, E., Behrenfeld, M. J., Westberry, T. K., & Sarmiento, J. L. (2020). Seasonal modulation of phytoplankton biomass in the Southern Ocean. *Nature Communications*, *11*(1), 5364. https://doi.org/10.1038/s41467-020-19157-2

Arteaga, L., Haëntjens, N., Boss, E., Johnson, K. S., & Sarmiento, J. L. (2018). Assessment of export efficiency equations in the Southern Ocean applied to satellite-based net primary production. *Journal of Geophysical Research: Oceans*, *123*(4), 2945–2964. https://doi.org/10.1002/2018JC013787

Bach, L. T., Stange, P., Taucher, J., Achterberg, E. P., Algueró-Muñiz, M., Horn, H., et al. (2019). The influence of plankton community structure on sinking velocity and remineralization rate of marine aggregates. *Global Biogeochemical Cycles*, *33*(8), 971–994. https://doi.org/10.1029/2019GB006256

Behrenfeld, M. J., & Boss, E. S. (2014). Resurrecting the ecological underpinnings of ocean plankton blooms. *Annual Review of Marine Science*, *6*(1), 167–194. https://doi.org/10.1146/annurev-marine-052913-021325

Belcher, A., Henson, S. A., Manno, C., Hill, S. L., Atkinson, A., Thorpe, S. E., et al. (2019). Krill faecal pellets drive hidden pulses of particulate organic carbon in the marginal ice zone. *Nature Communications*, *10*(1), 889. https://doi.org/10.1038/s41467-019-08847-1

Belcher, A., Iversen, M., Manno, C., Henson, S. A., Tarling, G. A., & Sanders, R. (2016). The role of particle associated microbes in remineralization of fecal pellets in the upper mesopelagic of the Scotia Sea, Antarctica. *Limnology & Oceanography*, *61*(3), 1049–1064. https://doi.org/10.1002/lno.10269

Biddle, L. C., & Swart, S. (2020). The observed seasonal cycle of submesoscale processes in the Antarctic marginal ice zone. *Journal of Geophysical Research: Oceans*, *125*(6). https://doi.org/10.1029/2019JC015587

Biggs, T. E. G., Huisman, J., & Brussaard, C. P. D. (2021). Viral lysis modifies seasonal phytoplankton dynamics and carbon flow in the Southern Ocean. *The ISME Journal*, *15*(12), 3615–3622. https://doi.org/10.1038/s41396-021-01033-6

Boyd, P. W., Claustre, H., Levy, M., Siegel, D. A., & Weber, T. (2019). Multi-faceted particle pumps drive carbon sequestration in the ocean. *Nature*, *568*(7752), 327–335. https://doi.org/10.1038/s41586-019-1098-2

Boyd, P. W., Strzepek, R., Takeda, S., Jackson, G., Wong, C. S., McKay, R. M., et al. (2005). The evolution and termination of an iron-induced mesoscale bloom in the northeast subarctic Pacific. *Limnology & Oceanography*, *50*(6), 1872–1886. https://doi.org/10.4319/lo.2005.50.6.1872

Briggs, N., Perry, M. J., Cetinić, I., Lee, C., D'Asaro, E., Gray, A. M., & Rehm, E. (2011). High-resolution observations of aggregate flux during a sub-polar North Atlantic spring bloom. *Deep Sea Research Part I: Oceanographic Research Papers*, *58*(10), 1031–1039. https://doi.org/10.1016/j.dsr.2011.07.007

Buesseler, K. O., & Boyd, P. W. (2009). Shedding light on processes that control particle export and flux attenuation in the twilight zone of the open ocean. *Limnology & Oceanography*, *54*(4), 1210–1232. https://doi.org/10.4319/lo.2009.54.4.1210

Buesseler, K. O., Boyd, P. W., Black, E. E., & Siegel, D. A. (2020). Metrics that matter for assessing the ocean biological carbon pump. *Proceedings of the National Academy of Sciences*, *117*(18), 9679–9687. https://doi.org/10.1073/pnas.1918114117

Carranza, M. M., & Gille, S. T. (2015). Southern Ocean wind-driven entrainment enhances satellite chlorophyll-a through the summer. *Journal of Geophysical Research: Oceans*, *120*(1), 304–323. https://doi.org/10.1002/2014JC010203

Cavan, E. L., Le Moigne, F. A. C., Poulton, A. J., Tarling, G. A., Ward, P., Daniels, C. J., et al. (2015). Attenuation of particulate organic carbon flux in the Scotia Sea, Southern Ocean, is controlled by zooplankton fecal pellets. *Geophysical Research Letters*, *42*(3), 821–830. https://doi.org/10.1002/2014GL062744

Cavan, E. L., Giering, S. L. C., Wolff, G. A., Trimmer, M., & Sanders, R. (2018). Alternative particle formation pathways in the eastern tropical North Pacific's biological carbon pump. *Journal of Geophysical Research: Biogeosciences*, *123*(7), 2198–2211. https://doi.org/10.1029/2018JG004392

Cetinić, I., Perry, M. J., D'Asaro, E., Briggs, N., Poulton, N., Sieracki, M. E., & Lee, C. M. (2015). A simple optical index shows spatial and temporal heterogeneity in phytoplankton community composition during the 2008 North Atlantic Bloom Experiment. *Biogeosciences*, *12*(7), 2179–2194. https://doi.org/10.5194/bg-12-2179-2015

Condie, S. (1999). Settling regimes for non-motile particles in stratified waters. *Deep Sea Research Part I: Oceanographic Research Papers*, *46*(4), 681–699. https://doi.org/10.1016/S0967-0637(98)00085-5

D'Asaro, E. A. (2008). Convection and the seeding of the North Atlantic bloom. *Journal of Marine Systems*, *69*(3–4), 233–237. https://doi.org/10.1016/j.jmarsys.2005.08.005

de Boyer Montégut, C. (2004). Mixed layer depth over the global ocean: An examination of profile data and a profile-based climatology. *Journal of Geophysical Research*, *109*(C12), C12003. https://doi.org/10.1029/2004JC002378

Fauchereau, N., Tagliabue, A., Bopp, L., & Monteiro, P. M. S. (2011). The response of phytoplankton biomass to transient mixing events in the Southern Ocean. *Geophysical Research Letters*, *38*(17). https://doi.org/10.1029/2011GL048498

Fitch, D. T., & Moore, J. K. (2007). Wind speed influence on phytoplankton bloom dynamics in the Southern Ocean marginal ice zone. *Journal of Geophysical Research*, *112*(C8), C08006. https://doi.org/10.1029/2006JC004061

Giddy, I., Swart, S., du Plessis, M., Thompson, A. F., & Nicholson, S. (2021). Stirring of Sea-Ice meltwater enhances submesoscale fronts in the Southern Ocean. *Journal of Geophysical Research: Oceans*, *126*(4). https://doi.org/10.1029/2020JC016814

Giering, S. L. C., Sanders, R., Lampitt, R. S., Anderson, T. R., Tamburini, C., Boutrif, M., et al. (2014). Reconciliation of the carbon budget in the ocean's twilight zone. *Nature*, *507*(7493), 480–483. https://doi.org/10.1038/nature13123

Graff, J. R., Westberry, T. K., Milligan, A. J., Brown, M. B., Dall'Olmo, G., Dongen-Vogels, V. v., et al. (2015). Analytical phytoplankton carbon measurements spanning diverse ecosystems. *Deep Sea Research Part I: Oceanographic Research Papers*, *102*, 16–25. https://doi.org/10.1016/j.dsr.2015.04.006

Hague, M., & Vichi, M. (2021). Southern Ocean Biogeochemical Argo detect under-ice phytoplankton growth before sea ice retreat. *Biogeosciences*, *18*(1), 25–38. https://doi.org/10.5194/bg-18-25-2021

Henson, S., Briggs, N., Carvalho, F., Manno, C., Mignot, A., & Thomalla, S. (2023). A seasonal transition in biological carbon pump efficiency in the northern Scotia Sea, Southern Ocean. *Deep Sea Research Part II: Topical Studies in Oceanography*, *208*, 105274. https://doi.org/10.1016/j.dsr2.2023.105274

Henson, S., Cael, B. B., Allen, S. R., & Dutkiewicz, S. (2021). Future phytoplankton diversity in a changing climate. *Nature Communications*, *12*(1), 5372. https://doi.org/10.1038/s41467-021-25699-w

Henson, S., Le Moigne, F., & Giering, S. (2019). Drivers of carbon export efficiency in the Global Ocean. *Global Biogeochemical Cycles*, *33*(7), 891–903. https://doi.org/10.1029/2018GB006158

Hopkins, J., Henson, S. A., Painter, S. C., Tyrrell, T., & Poulton, A. J. (2015). Phenological characteristics of global coccolithophore blooms: Coccolithophore bloom phenology. *Global Biogeochemical Cycles*, *29*(2), 239–253. https://doi.org/10.1002/2014GB004919

Hoppema, M. (2004). Weddell Sea is a globally significant contributor to deep-sea sequestration of natural carbon dioxide. *Deep Sea Research Part I: Oceanographic Research Papers*, *51*(9), 1169–1177. https://doi.org/10.1016/j.dsr.2004.02.011

Johnson, K. S., Plant, J. N., Coletti, L. J., Jannasch, H. W., Sakamoto, C. M., Riser, S. C., et al. (2017). Biogeochemical sensor performance in the SOCCOM profiling float array. *Journal of Geophysical Research: Oceans*, *122*(8), 6416–6436. https://doi.org/10.1002/2017JC012838

Johnson, K. S., Riser, S. C., Talley, L. D., Sarmiento, J. L., Swift, D. D., Plant, J. N., et al. (2022). SOCCOM float data - snapshot 2022-05-19. In *Southern Ocean carbon and climate observations and modeling (SOCCOM) float data archive*. UC San Diego Library Digital Collections. https://doi.org/10.6075/J0MC905G

Kauko, H. M., Hattermann, T., Ryan-Keogh, T., Singh, A., de Steur, L., Fransson, A., et al. (2021). Phenology and environmental control of phytoplankton blooms in the Kong Håkon VII Hav in the Southern Ocean. *Frontiers in Marine Science*, *8*, 623856. https://doi.org/10.3389/fmars.2021.623856

Klunder, M., Laan, P., Middag, R., De Baar, H., & van Ooijen, J. (2011). Dissolved iron in the Southern Ocean (Atlantic sector). *Deep Sea Research Part II: Topical Studies in Oceanography*, *58*(25–26), 2678–2694. https://doi.org/10.1016/j.dsr2.2010.10.042

Krause, J. W., Schulz, I. K., Rowe, K. A., Dobbins, W., Winding, M. H. S., Sejr, M. K., et al. (2019). Silicic acid limitation drives bloom termination and potential carbon sequestration in an Arctic bloom. *Scientific Reports*, *9*(1), 8149. https://doi.org/10.1038/s41598-019-44587-4

Kwiatkowski, L., Torres, O., Bopp, L., Aumont, O., Chamberlain, M., Christian, J. R., et al. (2020). Twenty-first century ocean warming, acidification, deoxygenation, and upper-ocean nutrient and primary production decline from CMIP6 model projections. *Biogeosciences*, *17*(13), 3439–3470. https://doi.org/10.5194/bg-17-3439-2020

Lacour, L., Briggs, N., Claustre, H., Ardyna, M., & Dall'Olmo, G. (2019). The intraseasonal dynamics of the mixed layer pump in the subpolar North Atlantic ocean: A biogeochemical-argo float approach. *Global Biogeochemical Cycles*, *33*(3), 266–281. https://doi.org/10.1029/2018GB005997

Lannuzel, D., Vancoppenolle, M., van der Merwe, P., de Jong, J., Meiners, K., Grotti, M., et al. (2016). Iron in sea ice: Review and new insights. *Elementa: Science of the Anthropocene*, *4*, 000130. https://doi.org/10.12952/journal.elementa.000130

Lester, C. W., Wagner, T. J. W., McNamara, D. E., & Cape, M. R. (2021). The influence of meltwater on phytoplankton blooms near the Sea-Ice edge. *Geophysical Research Letters*, *48*(2). https://doi.org/10.1029/2020GL091758

Li, Z., Lozier, M. S., & Cassar, N. (2021). Linking Southern Ocean mixed-layer dynamics to net community production on various timescales. *Journal of Geophysical Research: Oceans*, *126*(10). https://doi.org/10.1029/2021JC017537

Llort, J., Lévy, M., Sallée, J.-B., & Tagliabue, A. (2015). Onset, intensification, and decline of phytoplankton blooms in the Southern Ocean. *ICES Journal of Marine Science*, *72*(6), 1971–1984. https://doi.org/10.1093/icesjms/fsv053

MacGilchrist, G. A., Naveira Garabato, A. C., Brown, P. J., Jullion, L., Bacon, S., Bakker, D. C. E., et al. (2019). Reframing the carbon cycle of the subpolar Southern Ocean. *Science Advances*, *5*(8), eaav6410. https://doi.org/10.1126/sciadv.aav6410

Marsay, C. M., Sanders, R. J., Henson, S. A., Pabortsava, K., Achterberg, E. P., & Lampitt, R. S. (2015). Attenuation of sinking particulate organic carbon flux through the mesopelagic ocean. *Proceedings of the National Academy of Sciences*, *112*(4), 1089–1094. https://doi.org/10.1073/pnas.1415311112

Martin, J. H., Knauer, G. A., Karl, D. M., & Broenkow, W. W. (1987). VERTEX: Carbon cycling in the northeast Pacific. Deep sea research Part A. *Oceanographic Research Papers*, *34*(2), 267–285. https://doi.org/10.1016/0198-0149(87)90086-0

Massom, R. A., & Stammerjohn, S. E. (2010). Antarctic sea ice change and variability – Physical and ecological implications. *Polar Science*, *4*(2), 149–186. https://doi.org/10.1016/j.polar.2010.05.001

McPhee, M., & Morison, J. (2001). Under-ice boundary layer. In *Encyclopedia of ocean sciences* (pp. 3071–3078). Elsevier. https://doi.org/10.1006/rwos.2001.0146

Moreau, S., Boyd, P. W., & Strutton, P. G. (2020). Remote assessment of the fate of phytoplankton in the Southern Ocean sea-ice zone. *Nature Communications*, *11*(1), 3108. https://doi.org/10.1038/s41467-020-16931-0

Moreau, S., Hattermann, T., de Steur, L., Kauko, H. M., Ahonen, H., Ardelan, M., et al. (2023). Wind-driven upwelling of iron sustains dense blooms and food webs in the eastern Weddell Gyre. *Nature Communications*, *14*(1), 1303. https://doi.org/10.1038/s41467-023-36992-1

Naveira Garabato, A. C., MacGilchrist, G. A., Brown, P. J., Evans, D. G., Meijers, A. J. S., & Zika, J. D. (2017). High-latitude ocean ventilation and its role in Earth's climate transitions. *Philosophical Transactions of the Royal Society A: Mathematical, Physical & Engineering Sciences*, *375*(2102), 20160324. https://doi.org/10.1098/rsta.2016.0324

Nicholson, S.-A., Lévy, M., Jouanno, J., Capet, X., Swart, S., & Monteiro, P. M. S. (2019). Iron supply pathways between the surface and subsurface waters of the Southern Ocean: From winter entrainment to summer storms. *Geophysical Research Letters*, *46*(24), 14567–14575. https://doi.org/10.1029/2019GL084657

Nicholson, S.-A., Lévy, M., Llort, J., Swart, S., & Monteiro, P. M. S. (2016). Investigation into the impact of storms on sustaining summer primary productivity in the sub-Antarctic ocean: Storms sustain summer primary production. *Geophysical Research Letters*, *43*(17), 9192–9199. https://doi.org/10.1002/2016GL069973

Noh, Y., & Nakada, S. (2010). Estimation of the particle flux from the convective mixed layer by large eddy simulation. *Journal of Geophysical Research*, *115*(C5), C05007. https://doi.org/10.1029/2009JC005669

Omand, M. M., D'Asaro, E. A., Lee, C. M., Perry, M. J., Briggs, N., Cetinić, I., & Mahadevan, A. (2015). Eddy-driven subduction exports particulate organic carbon from the spring bloom. *Science*, *348*(6231), 222–225. https://doi.org/10.1126/science.1260062

Parkinson, C. L. (2019). A 40-y record reveals gradual Antarctic sea ice increases followed by decreases at rates far exceeding the rates seen in the Arctic. *Proceedings of the National Academy of Sciences*, *116*(29), 14414–14423. https://doi.org/10.1073/pnas.1906556116

Prend, C. J., Keerthi, M. G., Lévy, M., Aumont, O., Gille, S. T., & Talley, L. D. (2022). Sub-seasonal forcing drives year-to-year variations of Southern Ocean primary productivity. *Global Biogeochemical Cycles*, *36*(7). https://doi.org/10.1029/2022GB007329

Roesler, C., Uitz, J., Claustre, H., Boss, E., Xing, X., Organelli, E., et al. (2017). Recommendations for obtaining unbiased chlorophyll estimates from in situ chlorophyll fluorometers: A global analysis of WET Labs ECO sensors. *Limnology and Oceanography: Methods*, *15*(6), 572–585. https://doi.org/10.1002/lom3.10185

Sallée, J.-B., Pellichero, V., Akhoudas, C., Pauthenet, E., Vignes, L., Schmidtko, S., et al. (2021). Summertime increases in upper-ocean stratification and mixed-layer depth. *Nature*, *591*(7851), 592–598. https://doi.org/10.1038/s41586-021-03303-x

Schulz, K., Mohrholz, V., Fer, I., Janout, M., Hoppmann, M., Schaffer, J., & Koenig, Z. (2022). A full year of turbulence measurements from a drift campaign in the Arctic Ocean 2019–2020. *Scientific Data*, *9*(1), 472. https://doi.org/10.1038/s41597-022-01574-1

Smetacek, V., Klaas, C., Strass, V. H., Assmy, P., Montresor, M., Cisewski, B., et al. (2012). Deep carbon export from a Southern Ocean iron-fertilized diatom bloom. *Nature*, *487*(7407), 313–319. https://doi.org/10.1038/nature11229

Smith, W. O., & Comiso, J. C. (2008). Influence of sea ice on primary production in the Southern Ocean: A satellite perspective. *Journal of Geophysical Research*, *113*(C5), C05S93. https://doi.org/10.1029/2007JC004251

Smith, W. O., & Nelson, D. M. (1985). Phytoplankton bloom produced by a receding ice edge in the Ross Sea: Spatial coherence with the density field. *Science*, *227*(4683), 163–166. https://doi.org/10.1126/science.227.4683.163

Stukel, M. R., Irving, J. P., Kelly, T. B., Ohman, M. D., Fender, C. K., & Yingling, N. (2023). Carbon sequestration by multiple biological pump pathways in a coastal upwelling biome. *Nature Communications*, *14*(1), 2024. https://doi.org/10.1038/s41467-023-37771-8

Tagliabue, A., Sallée, J.-B., Bowie, A. R., Lévy, M., Swart, S., & Boyd, P. W. (2014). Surface-water iron supplies in the Southern Ocean sustained by deep winter mixing. *Nature Geoscience*, *7*(4), 314–320. https://doi.org/10.1038/ngeo2101

Taylor, M. H., Losch, M., & Bracher, A. (2013). On the drivers of phytoplankton blooms in the Antarctic marginal ice zone: A modeling approach: Marginal ice zone phytoplankton blooms. *Journal of Geophysical Research: Oceans*, *118*(1), 63–75. https://doi.org/10.1029/2012JC008418

Thomalla, S. J., Fauchereau, N., Swart, S., & Monteiro, P. M. S. (2011). Regional scale characteristics of the seasonal cycle of chlorophyll in the Southern Ocean. *Biogeosciences*, *8*(10), 2849–2866. https://doi.org/10.5194/bg-8-2849-2011

Timmermans, M.-L., Cole, S., & Toole, J. (2012). Horizontal density structure and restratification of the Arctic ocean surface layer. *Journal of Physical Oceanography*, *42*(4), 659–668. https://doi.org/10.1175/JPO-D-11-0125.1

Tréguer, P., Bowler, C., Moriceau, B., Dutkiewicz, S., Gehlen, M., Aumont, O., et al. (2018). Influence of diatom diversity on the ocean biological carbon pump. *Nature Geoscience*, *11*(1), 27–37. https://doi.org/10.1038/s41561-017-0028-x

Uchida, T., Balwada, D., Abernathey, R., McKinley, G., Smith, S., & Lévy, M. (2019). The contribution of submesoscale over mesoscale eddy iron transport in the open Southern Ocean. *Journal of Advances in Modeling Earth Systems*, *11*(12), 3934–3958. https://doi.org/10.1029/2019MS001805

Uchida, T., Balwada, D., Abernathey, R., Prend, C. J., Boss, E., & Gille, S. T. (2019). Southern Ocean phytoplankton blooms observed by biogeochemical floats. *Journal of Geophysical Research: Oceans*, *124*(11), 7328–7343. https://doi.org/10.1029/2019JC015355

von Berg, L., Prend, C. J., Campbell, E. C., Mazloff, M. R., Talley, L. D., & Gille, S. T. (2020). Weddell Sea phytoplankton blooms modulated by sea ice variability and polynya formation. *Geophysical Research Letters*, *47*(11). https://doi.org/10.1029/2020GL087954

Westberry, T., Behrenfeld, M. J., Siegel, D. A., & Boss, E. (2008). Carbon-based primary productivity modeling with vertically resolved photoacclimation:Carbon-based Porduction Model. *Global Biogeochemical Cycles*, *22*(2). https://doi.org/10.1029/2007GB003078

Wilson, E. A., Riser, S. C., Campbell, E. C., & Wong, A. P. S. (2019). Winter upper-ocean stability and ice–ocean feedbacks in the sea ice–covered Southern Ocean. *Journal of Physical Oceanography*, *49*(4), 1099–1117. https://doi.org/10.1175/JPO-D-18-0184.1

References From the Supporting Information

Behrenfeld, M. J., Boss, E., Siegel, D. A., & Shea, D. M. (2005). Carbon-based ocean productivity and phytoplankton physiology from space: Phytoplankton growth rates and ocean productivity. *Global Biogeochemical Cycles*, *19*(1). https://doi.org/10.1029/2004GB002299

Fetterer, F. K. K. M. W. S. M. W. A. (2017). *Sea Ice Index, Version 3*. NSIDC: National Snow and Ice Data Center. https://doi.org/10.7265/N5K072F8

Gregor, L., Ryan-Keogh, T. J., Nicholson, S.-A., du Plessis, M., Giddy, I., & Swart, S. (2019). GliderTools: A Python toolbox for processing underwater glider data. *Frontiers in Marine Science*, *6*, 738. https://doi.org/10.3389/fmars.2019.00738

Hersbach, H., Bell, B., Berrisford, P., Biavati, G., Horányi, A., Muñoz Sabater, J., et al. (2018). *ERA5 hourly data on single levels from 1979 to present*. Copernicus Climate Change Service (C3S) Climate Data Store (CDS).

Huntemann, M., Heygster, G., Kaleschke, L., Krumpen, T., Mäkynen, M., & Drusch, M. (2014). Empirical sea ice thickness retrieval during the freeze-up period from SMOS high incident angle observations. *The Cryosphere*, *8*(2), 439–451. https://doi.org/10.5194/tc-8-439-2014

Lavergne, T., Sørensen, A. M., Kern, S., Tonboe, R., Notz, D., Aaboe, S., et al. (2019). Version 2 of the EUMETSAT OSI SAF and ESA CCI sea-ice concentration climate data records. *The Cryosphere*, *13*(1), 49–78. https://doi.org/10.5194/tc-13-49-2019

McDougall, T. J., & Barker, P. M. (2011). In T. J. McDougall (Ed.), *Getting started with TEOS-10 and the Gibbs seawater (GSW) Oceanographic Toolbox*. Battery Point, Tas.

OSI-430-b. (2019). *Global sea-ice concentration interim climate data record 2016 onwards (v2.0), [Online]. EUMETSAT Ocean and sea-ice Satellite Application Facility*. Norwegian and Danish Meteorological Institutes.

OSI-450. (2017). *Global sea-ice concentration climate data record 1979-2015 (v2.0), [Online]. EUMETSAT Ocean and sea-ice Satellite Application Facility*. Norwegian and Danish Meteorological Institutes. https://doi.org/10.15770/EUM_SAF_OSI_0008

Platt, T., & Sathyendranath, S. (1993). Estimators of primary production for interpretation of remotely sensed data on ocean color. *Journal of Geophysical Research*, *98*(C8), 14561. https://doi.org/10.1029/93JC01001

Sathyendranath, S., Brewin, R., Brockmann, C., Brotas, V., Calton, B., Chuprin, A., et al. (2019). An Ocean-colour time series for use in climate studies: The experience of the ocean-colour climate change initiative (OC-CCI). *Sensors*, *19*(19), 4285. https://doi.org/10.3390/s19194285

Thomalla, S. J., Ogunkoya, A. G., Vichi, M., & Swart, S. (2017). Using optical sensors on gliders to estimate phytoplankton carbon concentrations and chlorophyll-to-carbon ratios in the Southern Ocean. *Frontiers in Marine Science*, *4*, 34. https://doi.org/10.3389/fmars.2017.00034

Zhang, X., Hu, L., & He, M.-X. (2009). Scattering by pure seawater: Effect of salinity. *Optics Express*, *17*(7), 5698. https://doi.org/10.1364/OE.17.005698